

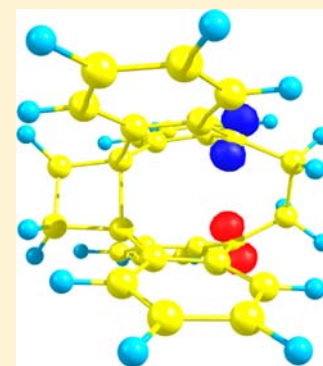
Volume Change during Thermal [4 + 4] Cycloaddition of [2.2] (9,10)Anthracenophane

Brad Slepetz and Miklos Kertesz*

Department of Chemistry, Georgetown University, 37th and O Streets, NW, Washington, D.C. 20057-1227, United States

S Supporting Information

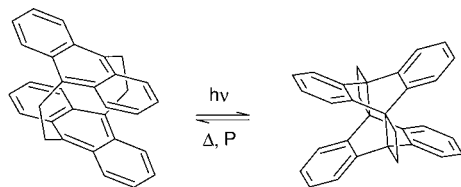
ABSTRACT: We show that the reaction path connecting the tethered bi(anthracene-9,10-dimethylene) and its photodimer proceeds stepwise via a diradicaloid transition state where one σ -bond is made before a second. The newly found transition state (TS) has a smaller molecular volume than either the reactant or the product giving an atomistic explanation to the recently found pressure catalyzed barrier lowering and rate enhancement. The density functional methods used include long-range contributions as required in a system where the dispersion interactions are significant. We discuss this transformation in the context of the diamond-to-graphite transition owing to the similarity of σ -bond breakage into a delocalized π -system. We also comment on the controversy surrounding the equilibrium geometries of photoisomerized cyclophanes, concluding that D_{2h} symmetry in the photoisomer of the title molecule is a transition structure connecting a pair of degenerate ground state D_2 geometries.



INTRODUCTION

In a surprising experiment¹ Jezowski et al. showed that the application of mechanical pressure significantly reduces the barrier for the thermal cycloaddition of bi(anthracene-9,10-dimethylene) (Scheme 1). In the Zeonex (polycycloolefin)

Scheme 1. [4 + 4] Cycloaddition of Bi(anthracene-9,10-dimethylene)^a



^aThe reaction is reversible under ambient conditions, and the reverse reaction is catalyzed by pressure.¹

polymer matrix, the activation energy for the dissociation of the photoisomer was reduced from 93 kJ mol⁻¹ at ambient pressure to 7 kJ mol⁻¹ under 0.9 GPa applied pressure. Typically much higher pressures around 10–20 GPa^{2–4} are needed to break bonds, and generally a negative activation volume signals bond formation and not bond breaking as discussed by Jezowski et al.¹ The authors hypothesized that the transition structure that connects the title compound with its photoisomer would show a smaller molecular volume than either equilibrium structure. Here we explore the potential energy surface of the thermal cycloaddition reaction to answer the question: Is there a transition structure (TS) or intermediate to be found on the potential energy surface that can provide an atomistic interpretation for this new experimental result?

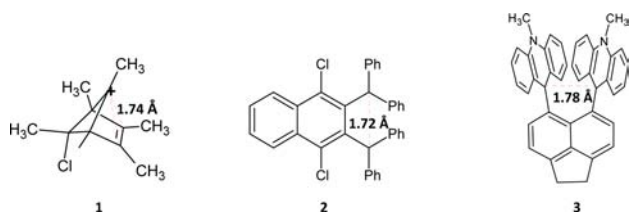
A second motivation for finding an accurate reaction path for this reaction derives from the interest in interatomic contacts between carbon atoms in the range 1.7–2.8 Å. These contact values are uncommon but not unprecedented⁵ and continue to attract interest.⁶ Note that the X-ray crystal structure data for the title compound and its photoisomer show that the critical CC contacts are⁷ $d(1-2) = 2.765$ Å and $d(1-2) = 1.653$ Å, respectively. One of the motivations of this study is to see whether a reaction intermediate can be identified with CC contacts closer to the “forbidden” 2.0–2.5 Å range.

Special structural and electronic peculiarities⁸ such as strain, steric hindrance, ionic charge, and radical character are necessary to generate long CC bonds >1.65 Å or short CC contacts <2.9 Å. Electron deficient carbocations are known^{9,10} to interact with electron rich π -bonds to form a three-center, two electron homoaromatic bond with CC distances in the 1.6–1.75 Å range as in **1**.¹¹ Neutral sp³–sp³ bond lengths >1.7 Å have been observed in benzocyclobutane derivatives,¹² as in **2**. Here, the steric crowding of the phenyl groups forces the respective CC bond to a greater distance where a long σ -bond is preferred over a diradical state. 1,1,2,2-Tetraarylpyracene (**3**) has a long CC σ -bond with two distinct distances, 1.71 and 1.78 Å, due to two crystallographically independent molecules in the unit cell.¹³

Paracyclophanes, another example containing unusual CC distances, are of chemical interest due to their unconventional structures and photoisomerization reactivities.^{14,15} Applications in the fields of chiral catalysis,^{16,17} electronic materials,¹⁸ and optical switches¹⁹ have broadened this interest. Structural anomalies in paracyclophanes include nonplanar distorted

Received: March 9, 2013

Published: August 8, 2013



aromatic rings and unusual distances between sp^3 -hybridized carbons. While the structure of paracyclophanes has been studied experimentally^{20–23} and theoretically^{24–29} with a variety of methods, the reaction paths of photoisomerization have been largely ignored. Bi(anthracene-9,10-dimethylene) (**4**) can form a photodimer (**5**) through an intramolecular [4 + 4] cycloaddition (Figure 1) in which the central aromatic rings

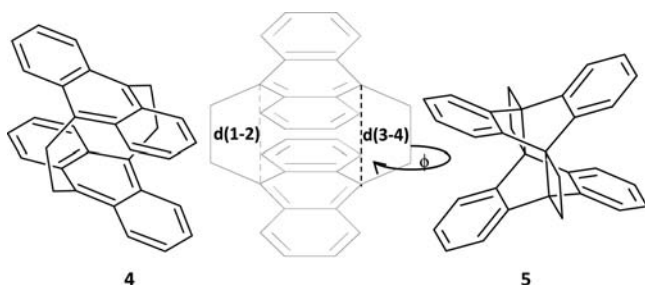


Figure 1. Bi(anthracene-9,10-dimethylene) (left, **4**) with the distance $d(1-2)/d(3-4)$ labeled (center) that undergoes the greatest geometrical change during isomerization. The photodimer **5** is shown at right. The torsion ϕ correlates with $d(1-2)$ and may be parallel or twisted relative to the torsion on the opposite side.

connect via an sp^2 – sp^3 transition. Other photodimers, of the Diels–Alder [4 + 2] variety, might be formed under high pressure without photoexcitation.³⁰ We also note the analogy of cycloaddition to the diamond-to-graphite transition; as the paracyclophane undergoes intramolecular isomerization, the distance $d(1-2)$ (Figure 1) decreases, breaking the aromaticity of the connecting rings, forming an elongated electron pair σ -bond.

Bi(anthracene-9,10-dimethylene) is of particular interest because the anthracene unit, with its three aromatic rings, can aid in the stabilization of intermediate structures during photoisomerization. **4** isomerizes to **5** in a thermally forbidden, photochemically allowed [4 + 4] cycloaddition (Scheme 1). The reverse, bond dissociative reaction (**5** → **4**) can be accelerated by hydrostatic pressure leading to the notion that the TS has a smaller volume than the photoisomer **5** or the clamped bisanthracene **4**.¹ This study presents the computational modeling for the reverse **5** → **4** because the experimental data refer to this dark reaction.¹

X-ray data indicate that **4** (CSD refcode: ANTMET05⁷) has $d(1-2) = 2.765$ Å and **5** (CSD refcode: ANTMEU03⁷) has $d(1-2) = 1.653$ Å. As cycloaddition proceeds, the central ring transforms from a nearly planar sp^2 -hybridized aromatic system to a nonplanar system with $d(1-2)$ bonding two sp^3 -hybridized carbons. This process spans the distances that are encountered, as graphite is compressed into diamond. We will present two pathways for the ground state photoisomerization of bi(anthracene-9,10-dimethylene) and discuss these in the context of the diamond-to-graphite transformation. We have explored the potential energy surface (PES) and find detailed information for two competing pathways that involve the

breaking of the $d(1-2)/d(3-4)$ pair of bonds: one in which they break in synch and another where one pair breaks before the other.

METHODOLOGY

All molecular calculations were performed with the Gaussian 09³¹ suite using the M06-2x³² and Grimme's B97D³³ density functionals paired with various Gaussian split-valence³⁴ basis sets. The accuracy of the M06-2x model chemistry applied to reproducing the geometric parameters of small paracyclophanes was previously demonstrated by Bachrach²⁹ using the split-valence triple- ζ basis 6-311G(d,p). Quenneville and Germann used extensive DFT calculations with 6-31G(d) for exploring the potential energy surfaces of benzene and anthracene dimers under pressure.³⁰ Our test calculations with the 6-31G(d,p) basis set on **4** and **5** showed minute geometrical changes with distances within 0.001 Å. The difference in ΔE between these species from the 6-311G(d,p) basis to the smaller 6-31G(d,p) was 0.2 kcal mol⁻¹. We therefore use the smaller basis set in this work. M06-2x and B97D were chosen because medium range electron correlation effects are important for interacting conjugated substructures. Energy minima and maxima were confirmed through vibrational analysis ensuring only real frequencies for minima and exactly one imaginary frequency for transition structures. Transition structures were searched for by quadratic synchronous transit³⁵ (QST) and were connected to energy minima by following the amplitude of the imaginary frequency as implemented in the intrinsic reaction coordinate³⁶ (IRC) method. Molecular volumes were calculated from the electron density by the method described by Wong et al.³⁷ in which the volume is defined as that within a 0.001 electron/Bohr³ contour, estimated with a Monte Carlo integration. A total of 100 iterations were used with the number of integration points per cubic bohr chosen to obtain a total of approximately 10 000 integration points, as demonstrated in previous studies.^{1,38}

For solid state calculations, the augmented plane wave electronic structure code PWscf—part of the Quantum ESPRESSO³⁹ package—was used to perform self-consistent field (SCF) total energy calculations on the rhombohedral structures. We use the exchange correlation functional of Perdew et al. (PBE).⁴⁰ The structure is defined by three independent parameters as shown in Figure 2: the

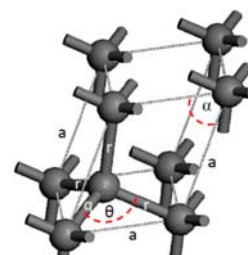


Figure 2. Schematic representation of the parameters involved in the diamond-to-graphite transition. r is the in-plane bond length, q is the interlayer separation, and θ is the interlayer angle.

interlayer separation q , unit cell length a , and the interaxes angle α . The values of these parameters are what determine the in-plane bond length r and the interlayer angle θ . The diamond and graphite structures were fully optimized such that the atoms and cell parameters were permitted to relax to minimize the energy. Note that due to the lack of long-range dispersion in the PBE functional, the interlayer interactions at the graphite end are not well represented. All other structures along the path were constructed with the separation of the atoms q taken as a given starting point, and the cell parameters a and α were varied until a local minimum was obtained. The optimized parameters for diamond, graphite, and the transition state are summarized in the Supporting Information. For all calculations, the kinetic energy cutoff of the plane waves was 48.0 Ry with a charge density cutoff of 348 Ry. Electron SCF convergence was set at 10^{-8}

within a $16 \times 16 \times 16$ Monkhorst–Pack Brillion zone sample grid, and Fermi–Dirac electron smearing of 10^{-3} Ry was used. A Vanderbilt ultrasoft pseudopotential, parametrized for small organic molecules by Meyer,⁴¹ was used to treat the carbon core electrons. For the full geometric optimizations, convergence was satisfied when the total energy change between successive steps was less than 10^{-7} E_H and the components of all the forces on the atoms were reduced below 51 meV/Å.

DIAMOND-TO-GRAPHITE TRANSITION

The modeling of the diamond-to-graphite transition is simplified^{42,43} when using a two atom rhombohedral cell in which the first carbon atom lies at the origin at a distance q from the second carbon, aligned along the z -axis. This cell allows a smooth transition from diamond to ABC graphite and is described (Figure 2) by three parameters: the in-plane bond length r , the interlayer distance q , and the interlayer angle θ . Ideally diamond has $q = r = 1.54$ Å with $\theta = 109.5^\circ$. As q increases toward graphite, r decreases as π -electron delocalization develops.

Table S1 contains the parameters as calculated in this work for diamond, graphite, and the structure with highest energy along the synchronous transition. Figure 3 shows the energy

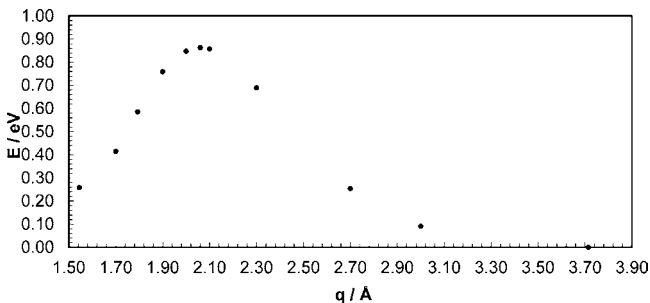


Figure 3. Relaxed scan of the total energy per unit cell for the diamond-to-graphite transition along the interplanar distance q using DFT band theory. The transition structure (TS) is at $q = 2.06$ Å.

profile for the diamond-to-graphite transition as a function of q . The transition structure is at $q = 2.06$ Å with $r = 1.47$ Å and $\theta = 102^\circ$. Unrestricted formalism at this geometry did not lower the energy as neither a spin-triplet or diradical state was found. This point is worth discussing further. The lack of splitting of α and β orbitals is an indication that instead of developing localized spins when the σ -bonds break, the system gains energy by forming delocalized π -like orbitals. Given the pyramidalization angle of $\theta = 102^\circ$ it is not surprising that the electronic structure undergoes a rearrangement without such spin symmetry breaking. Typically, a larger exact exchange component in a hybrid DFT leads to a wider range of geometrical parameters with spin symmetry breaking. The maximum propensity to such broken symmetry solutions occurs with 100% exact exchange at UHF. After extensive efforts we found such a symmetry broken solution with UHF only with a minimal energy lowering of 0.9 kcal mol⁻¹ at $q = 2.1$ Å. This finding explains why at the PBE level we find no broken symmetry solution in the graphite-to-diamond transition.

The geometry at the TS along the graphite to diamond path discussed here is characterized by geometrical parameters that are not unexpected for a transition between a σ -bond and simultaneous delocalization of the resultant radical electrons into a delocalized π -electron system. Therefore, it is instructive to see how the various geometrical parameters change during

this transformation which will serve as a basis of comparison for the valence isomerization of the title compound. Figure 3 shows the energy profile for the diamond-to-graphite transition as a function of q where it is observed that the activation energy is about 0.6 eV/unit cell. This is only about 15% of the bond dissociation energy observed in CC σ -bonds in typical organic molecules,⁴⁴ highlighting the importance of delocalization in stabilizing bond breakage. The geometrical relaxation confirms this process. In Figure 4, the in-plane bond length is plotted

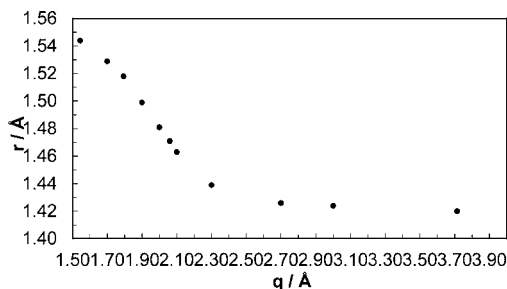


Figure 4. Change in the in-plane bond length r with interlayer separation, q . Data correspond to the relaxed scan in Figure 3.

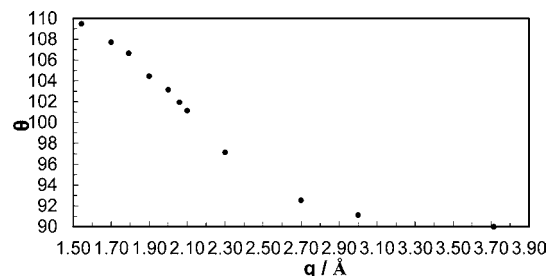


Figure 5. Change in the interplane angle θ with interplanar distance q for the diamond-to-graphite transition. Data correspond to the relaxed scan in Figure 3.

against q . Likewise, in Figure 5 the interplane angle θ is plotted against q . Both curves show a smooth transition from the sp^3 -hybrid parameters of 1.54 Å and 109.5° to the sp^2 -hybrid parameters of 1.41 Å and 90° indicating that the π -bonds develop parallel to the σ -bonds being broken. While the graphitic layers are still quite corrugated at the TS ($\theta = 102^\circ$) the in-plane bonds r are more than halfway at their final graphitic values.

VALENCE TAUTOMERS OF THE CYCLOPHANE BI(ANTHRACENE-9,10-DIMETHYLENE)

The energies and geometries of five relevant tautomers involved in the cycloaddition of bi(anthracene-9,10-dimethylene) are summarized in Table 1 for two model chemistries. In both models, the relative energies of the species follow the same order and the difference between the D_2 dissociated tautomer (4a) and the crystallographically observed C_2 structure (4b) is less than 1 kcal mol⁻¹. The largest difference between the two methods is the calculated dissociation reaction energy (5a-to-4a), which is exothermic at -9.11 kcal mol⁻¹ in M06-2x/6-31G(d,p) and -21.2 kcal mol⁻¹ in B97D/6-31+G(d). The B97D model is closer to the exothermic heat of reaction experimental value,⁴⁵ as measured by differential scanning calorimetry, of -35 to -39 kcal mol⁻¹. However,

Table 1. Relative Energies and Relevant Geometric Parameters for the Molecular Species Presented in This Work^a

| species | DFT | | M06-2x/6-31G(d,p) | | B97D/6-31+G(d) | | |
|----------------|----------|--------|-------------------|-----------------|----------------|----------|-----------------|
| | symm. | energy | $d(1-2)$ | $\phi(1-5-6-2)$ | energy | $d(1-2)$ | $\phi(1-5-6-2)$ |
| 4a | D_2 | 0 | 2.802 | 33.5 | 0 | 2.823 | 32.9 |
| 4b | C_2 | 0.75 | 2.814 | 20.5 | 0.43 | 2.826 | 19.5 |
| 5a | D_2 | 9.11 | 1.645 | 17.5 | 21.2 | 1.688 | 16.9 |
| 5b | D_{2h} | 13.8 | 1.645 | 0.2 | 24.5 | 1.689 | 0.0 |
| 6 ^b | C_2 | 36.9 | 1.692 | 17.4 | 36.8 | 1.814 | 17.5 |
| | | | 2.626 | 35.1 | | 2.609 | 32.4 |

^aEnergies in kcal mol⁻¹, distances in Å, and angles in deg. ^bEnergy minimum in M06-2x; TS in B97D.

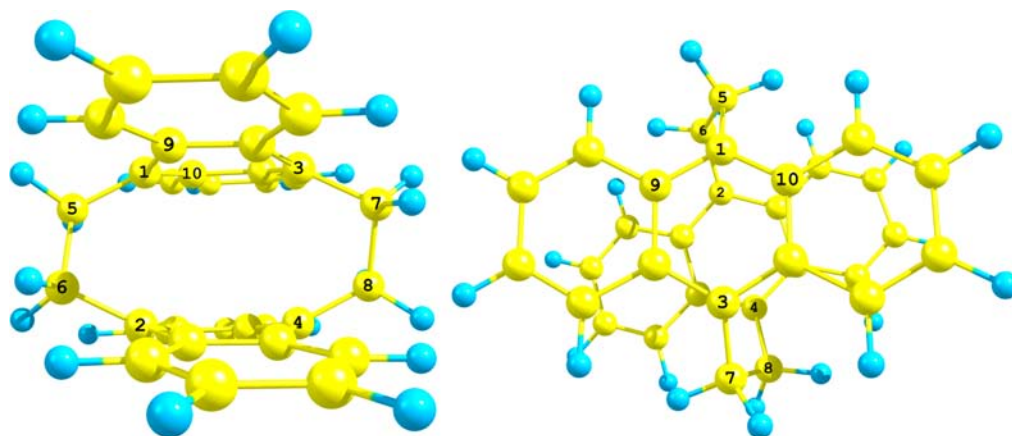


Figure 6. Two views of 4. $d(1-2)$ and $d(3-4)$ undergo the greatest change during isomerization to 5. The torsional angles $\phi(1-5-6-2)$ and $\phi(3-7-8-4)$ also change significantly.

M06-2x better predicts the reaction barrier energy (see text below).

Figure 6 illustrates the relevant CC distances that undergo the greatest change are $d(1-2)$ and $d(3-4)$.

Where these distances are unequal, $d(3-4)$ will refer to the longer of the two. For both model chemistries, the global minimum is found to have D_2 symmetry (4a) whereby the torsional angles of the bridging carbons twist relative to one another. An isomer with C_2 symmetry (4b)—observed with X-ray crystallography^{7,46,47}—is found to be less than 1 kcal mol⁻¹ above 4a (Figure 7). We found a transition structure linking these torsional isomers (not pictured) that is energetically only 1.35 kcal mol⁻¹ above 4a.

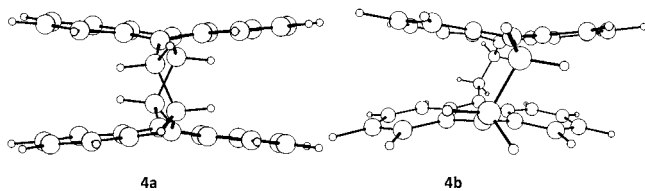


Figure 7. Bi(anthracene-9,10-dimethylene) with D_2 symmetry (left) and C_2 symmetry (right). 4a is calculated to be lower in energy by 0.75 kcal mol⁻¹ at the M06-2x/6-31G(d,p) level.

The crystal structure^{7,47-50} of the cycloaddition product, 9,9':10,10'-diethano-9,9':10,10'-bi-9,10-dihydroanthracene, has D_{2h} symmetry (5b), but we find this geometry to be 5 kcal mol⁻¹ higher than a structure possessing D_2 symmetry (5a) (Figure 8). The equilibrium geometry of smaller cyclophanes has been the subject of debate^{27,51,52} with X-ray diffraction data indicating a D_{2h} geometry for [2.2]paracyclophane with no

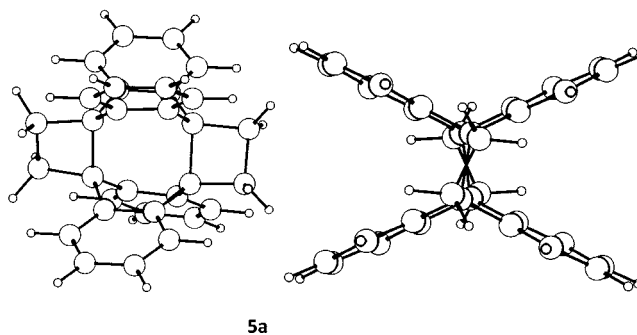


Figure 8. Two views of the optimized geometry of the cycloaddition product 5a (D_2 symmetry) at the M06-2x/6-31G(d,p) level.

twist. We find the D_{2h} structure to be a first-order saddle point on the PES connecting two degenerate D_2 isomers, as the carbon bridges twist relative to each other.

We also find a local minimum in M06-2x that has not been described before: it has broken symmetry (BS, 6) (Figure 9) with intermediate and unequal CC distances $d(1-2) = 1.69$ Å, $d(3-4) = 2.63$ Å. The BS tautomer ground state is a diradical with spin density localized on the long CC bonds and the only example we have found of a stationary point having a spin-unrestricted solution as all other species have closed shells. Structure 6 is key to understanding the full potential energy surface, and it corresponds to one of the bonds being broken while the other is stretched only slightly which will be discussed in the next section. A triplet ground state is competitive, calculated to be higher in energy by 0.6 kcal mol⁻¹ which should be contrasted with the calculations by Quenneville and Germann,³⁰ who found for the dimerization of untethered anthracene under high pressure that the triplet path is lower

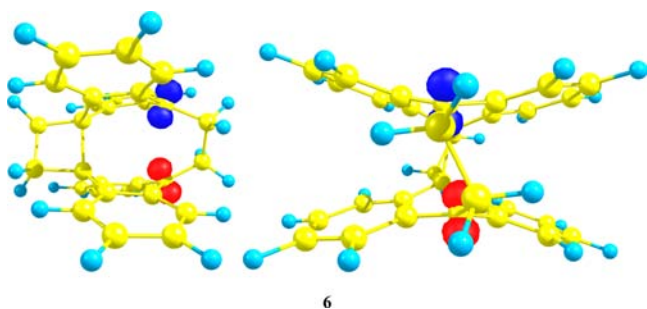


Figure 9. Two views of the broken-symmetry (6) tautomer at the M06-2x/6-31G(d,p) level showing where the bulk of the spin density is located at the long carbon-carbon contact sites. $d(1-2) = 1.69 \text{ \AA}$ (shown as a bond), $d(3-4) = 2.63 \text{ \AA}$ joins the radical sites.

than the singlet path for the asynchronous transit but overall the synchronous transit ends up being the lower barrier path.

■ PATHWAYS

We have calculated two PESs for the thermal cycloaddition transition, monitoring the changes in geometry, energy, and spin density (where applicable) to compare with the graphite-to-diamond transition. We start with a synchronous path in which $d(1-2) = d(3-4)$ along all points of the reaction. As shown in Figure 10, the cycloaddition transition proceeds

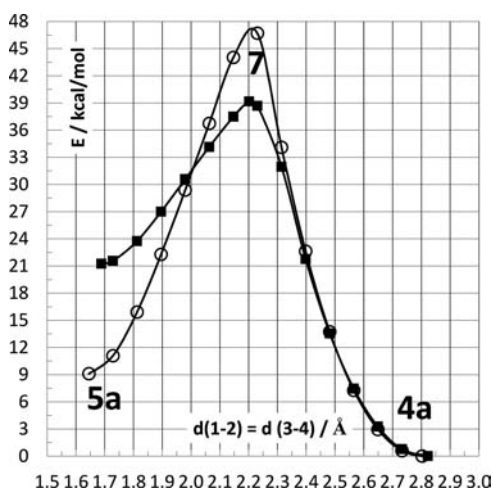


Figure 10. Total energy along the synchronous path for the cycloaddition of bi(anthracene-9,10-dimethylene) at the UM06-2x/6-31G(d,p) (O) and UB97D/6-31+G(d) (■) levels.

through a (left-to-right) barrier of 38 kcal mol^{-1} and is endothermic with a reaction energy of 9 kcal mol^{-1} in M06-2x/6-31G(d,p) model chemistry. All points along the path have closed shells except for the maximum at $d(1-2) = 2.20 \text{ \AA}$. A spin-restricted single-point energy calculation for this geometry is $9.95 \text{ kcal mol}^{-1}$ higher.

Vibrational analysis on the maximum energy structure 7 (Figure 11) reveals two imaginary modes: one with synchronous displacement among the pair of long carbon contacts and another that stretches the carbon contact pairs asymmetrically toward a structure that resembles the BS species 6. In B97D/6-31+G(d), the barrier is reduced due to a lower total energy for the transition state and a greater exothermic difference between equilibrium species.

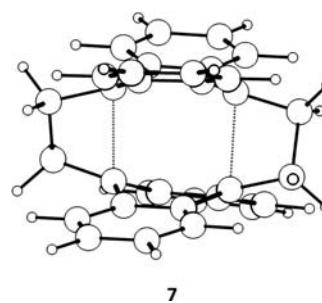


Figure 11. Structure of the second-order saddle point calculated for the synchronous path at $d(1-2) = 2.20 \text{ \AA}$ using the M06-2x/6-31G(d,p) level. Dashed lines indicate the short contacts between $d(1-2)$ and $d(3-4)$.

Figure 12 shows the change in the distances $d(1-9)$ and $d(1-10)$ calculated with M06-2x/6-31G(d,p) along the

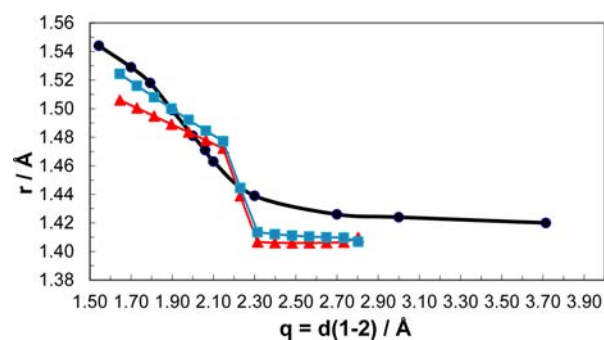


Figure 12. Change in the in-plane bond length r as a function of the interplane distance q in the diamond-to-graphite transition (black circles) overlaid with the analogous bond lengths in the synchronous transition of 5a to 4a. Blue squares refer to $d(1-9)$; red triangles refer to $d(1-10)$.

synchronous path, which are analogous to the in-plane bond length r in the diamond-to-graphite transition. In the latter case there is only one distance value with all in-plane bonds being equivalent. For each distance, two similar correlations are observed around the transition structure. Likewise, Figure 13 depicts the changes in angles $\theta(9-1-2)$ and $\theta(10-1-2)$ that are analogous to the diamond-to-graphite interplane angle. Here we find two different types of angles with $\theta(10-1-2)$ spanning 103° – 120° while $\theta(9-1-2)$ is more analogous to

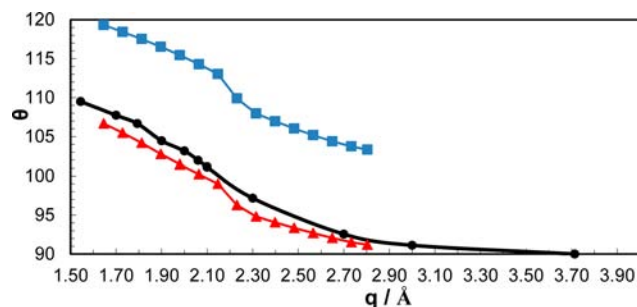


Figure 13. Change in the interlayer angle θ as a function of interplane distance q in the diamond-to-graphite transition (black circles) overlaid with the change in the analogous pair of angles in the synchronous transition of 5a to 4a. Blue squares refer to $\theta(10-1-2)$; red triangles refer to $\theta(9-1-2)$.

the sp^3/sp^2 diamond-to-graphite transition, following the close correlation between 91° and 107° .

We now consider the possibility of a pathway where $d(1-2)$ changes asymmetrically; that is, one bond forms in the cycloaddition before the other. Figure 13 shows such a pathway in ($d(1-2)$, $d(3-4)$) space based on our two model chemistries. For M06-2x, the asymmetric path passes through two transition states that flank a very shallow local minimum, **6** (BS). TS1 connects **5a** to **6** and lies just $0.2 \text{ kcal mol}^{-1}$ above **6**. TS2 connects **6** to **4a** and is 2 kcal mol^{-1} above **6**. In B97D, the equilibrium structures are connected by a single TS with no intermediate. It is an essential feature of this reaction that the lower barrier path in both model chemistries proceeds through a region close to structure **6** pointing to a stepwise process.

Figure 14 shows the variation in the parameters $d(1-2)/d(3-4)$ for both model chemistries. Starting at the equilibrium

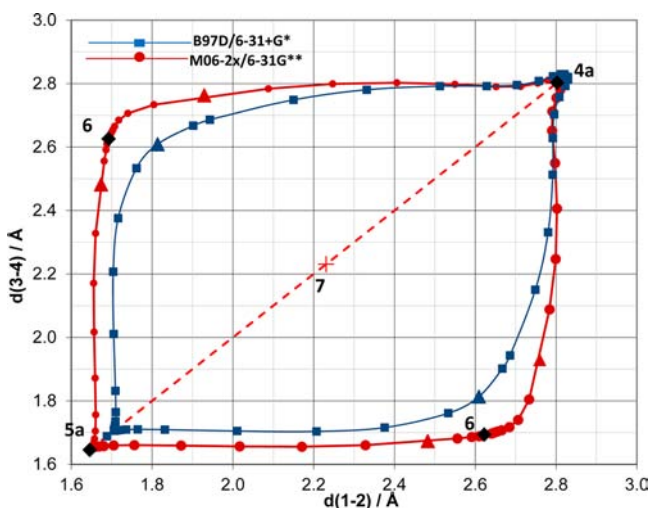


Figure 14. PES of the cycloaddition of bi(anthracene-9,10-dimethylene) with the two model chemistries used in this work in ($d(1-2)$, $d(3-4)$) space. Red circles follow the asynchronous path as calculated with UM06-2x/6-31G(d,p); blue squares follow the path calculated with UB97D/6-31+G*. Triangles indicate transition structures, and diamonds indicate minima. The red dashed line follows the synchronous path with the + indicating the location of the second-order saddle point found using M06-2x/6-31G(d,p).

photoisomer **5a** we see that for the synchronous path, $d(1-2)$ (blue circles), there remains a (long) σ -bond while $d(3-4)$ breaks (red squares) until the first transition state (TS1) at which point it begins to break. The dashed red line follows the synchronous path with $d(1-2) = d(3-4)$ which produced the energy profile given in Figure 10. In Figure 15, we show the change in $d(1-2)/d(3-4)$ for both paths calculated at the UM06-2x/6-31G(d,p) level. Here we see clearly that the barrier is higher for the synchronous path and that a lower barrier height is obtained by first breaking one pair of CC bonds before the other.

The full spin-unrestricted PES along the IRC for both models is shown in Figure 16. In M06-2x/6-31G(d,p), the reaction barrier of 28 kcal mol^{-1} compares favorably to the measured value of $24.0 \text{ kcal mol}^{-1}$ in a toluene solution⁴⁵ and $22.2 \text{ kcal mol}^{-1}$ in a polycycloolefin polymer matrix,¹ overshooting by $4-6 \text{ kcal mol}^{-1}$. The B97D/6-31+G(d) IRC model undershoots the experimental reaction barrier by $7-9 \text{ kcal mol}^{-1}$. The PES displays a diradicaloid character⁵³ in a narrow range at the BS (**6**) structure corresponding to one

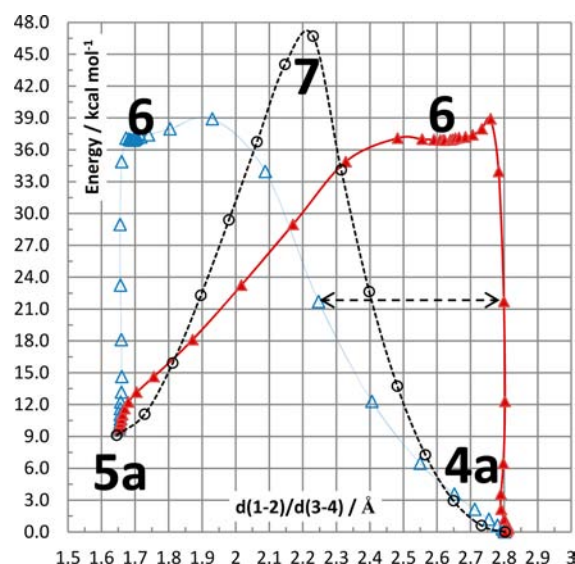


Figure 15. Change in the parameter $d(1-2)/d(3-4)$ for both thermal pathways discussed in this work calculated at the UM06-2x/6-31G(d,p) level. Blue (empty) and red (filled) triangles plot the changes in $d(1-2)$ and $d(3-4)$, respectively, in the asymmetric path. Note that initially $d(1-2)$ changes little as $d(3-4)$ elongates until the first transition state (TS1), at which point $d(1-2)$ breaks. The broken black line with circles follows the synchronous path where $d(1-2) = d(3-4)$ universally. A pair of corresponding $d(1-2)/d(3-4)$ values is indicated by the horizontal dashed line with arrows.

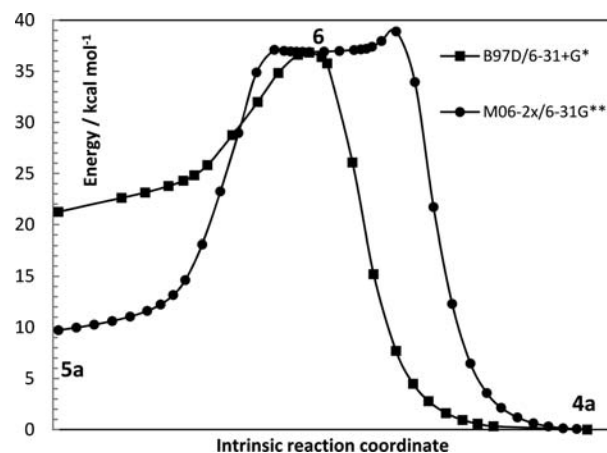


Figure 16. Total energy along the intrinsic reaction coordinate of Figure 14 for the asymmetric thermal cycloaddition pathway (left: **5a** to right: **4a**) calculated at the UB97D/6-31+G(d) (■) and UM06-2x/6-31G(d,p) (●) levels.

broken σ -bond as indicated by the spin density distribution shown in Figure 9. We calculate⁵⁴ the number of effectively unpaired electrons (NEUE) to be 1.58 with M06-2x and 1.42 with B97D (due to the difference in the amount of exchange) further indicating high diradical character. This is smaller than the value of 2.08 found in the second-order saddle point **7** in the synchronous path. It can then be argued that one of the reasons for the preference of the stepwise asynchronous path is that it minimizes the amount of high-energy diradical character. This intermediate is separated by small barriers on both sides to the two transition structures TS1 and TS2, and therefore in a practical sense the whole region around these structures behave as a transition state in the transformation.

VOLUME CHANGE DURING REACTION

Table 2 contains the calculated molecular volumes of the various species presented in this work with various model

Table 2. Molecular Volumes^a of the Various Species in This Work

| species | expt ^b | UB97D/6-31+G(d) | UM06-2x/6-31G(d,p) |
|---------|--------------------|-----------------|--------------------|
| 4a | – | 508.3 | 431.5 |
| 4b | 510.3 | 505.3 | 429.3 ^d |
| 5a | 506.5 ^c | 507.1 | 493.2 |
| 6 | – | 437.0 | 429.8 |
| 7 | – | 433.3 | 425.0 |

^aVolumes are in Å³. ^bX-ray structures taken from ref 7. ^cExperiment is on the D_{2h} structure (5b). ^dWhen diffuse functions are added, we obtain volumes of 501.2 and 505.5 for the basis sets 6-31+G(d) and 6-31+G(d,p), respectively.

chemistries. We found the need for the inclusion of diffuse functions in order to accurately match experimental X-ray volumes where available. This was particularly clear for 4b. For this reason we calculated the molecular volumes using a variety of basis sets at both DFTs. The calculated volumes of both transition structures 6 and 7 are the same within one standard deviation, giving credence to the proposed dissociation mechanism involving a TS with a smaller molecular volume.¹ The calculated volume change is about 15–19%, much larger than the ~3% obtained experimentally.¹ We expect this discrepancy to be largely due to the difference between the experiment in a polymer matrix, where reactant molecules are encapsulated, and the gas phase calculation. The reduction of the molecular volume is significant in the TS region fully supporting at the atomistic level the mechanism proposed by Jezowski et al.¹

CONCLUSIONS

The [4 + 4] cycloaddition in bi(anthracene-9,10-dimethylene) process has similarities to the diamond-to-graphite transition. We calculated two pathway PESSs, a synchronous change and an asymmetric change, and observe the sp³–sp² change during photoisomerization mimics the carbon allotropic change in some respects, among them being the complete absence of stationary points with nearest neighbor CC distances around 2.20 Å. In fact, this distance seems to be “off limits,” and we know of no molecule exhibiting this distance between sp³ carbons except in the crowded environment of cyclic compounds. The change in d₁₂ is subtle away from the transition structure but dramatic at 2.1 Å < d(1–2) < 2.3 Å, where it is clear that there is no geometry that can satisfy a minimum energy structure and instead we find transition structures in this range. By breaking (or completing) the bond separated by either d(1–2) or d(3–4) before the other, higher energy structures in which both of these distances must be near 2.3 Å simultaneously are circumvented and this asymmetric pathway reduces the barrier by 10 kcal mol^{–1} relative to the synchronous path. A diradical structure is found along the asymmetric path, near the transition, but whether this structure is a true minimum depends on the model chemistry used. Quenneville and Germann³⁰ noted that the lowest energy path is synchronous for the dimerization of anthracene at the 9 and 10 sites as here without the tethers present in this work although they also noticed a diradicaloid intermediate on the triplet surface. This is in contrast to our lowest energy path

which proceeds via a singlet diradicaloid asymmetrical (stepwise) intermediate. The effect of the tethers is to hold the pairs of the 9 and 10 sites in proximity during the reaction.

The molecular results inspire the thought that an alternative asymmetric-type path might be modeled in the diamond-to-graphite transition that passes through a smaller barrier compared to the simple synchronous path. The computed reduction of the molecular volume is significant in the TS region regardless of the applied density functional, fully supporting the pressure accelerated reaction mechanism proposed by Jezowski et al.¹

ASSOCIATED CONTENT

Supporting Information

Computational details, coordinates of optimized structures. This material is available free of charge via the Internet at <http://pubs.acs.org>.

AUTHOR INFORMATION

Corresponding Author

kertesz@georgetown.edu

Notes

The authors declare no competing financial interest.

ACKNOWLEDGMENTS

We thank the National Science Foundation for its support of this research (Grant No. CHE-1006702). We thank Ryan Vary for his preliminary computations on the graphite to diamond transition.

REFERENCES

- Jezowski, S. R.; Zhu, L.; Wang, Y.; Rice, A. P.; Scott, G. W.; Bardeen, C. J.; Chronister, E. L. *J. Am. Chem. Soc.* **2012**, *134*, 7459–7466.
- Wen, X.-D.; Hoffmann, R.; Ashcroft, N. W. *J. Am. Chem. Soc.* **2011**, *133*, 9023–9035.
- Beneditti, L. R.; Nguyen, J. H.; Caldwell, W. A.; Liu, H.; Kruger, M.; Jeanloz, R. *Science* **1999**, *286*, 100.
- Zeng, Q.; He, Z.; San, X.; Ma, Y.; Tian, F.; Cui, T.; Liu, B.; Zou, G.; Mao, H. *Proc. Natl. Acad. Sci. U.S.A.* **2008**, *105*, 4999–5001.
- Streek, J. *Acta Crystallogr., Sect. B* **2006**, *62*, 567–579.
- Fokin, A. A.; Chernish, L. V.; Gunchenko, G. A.; Tikhonchuk, E. Y.; Hausmann, H.; Serafin, M.; Dahl, J. E. P.; Carlson, R. M. K.; Schreiner, P. R. *J. Am. Chem. Soc.* **2012**, *134*, 13641–50.
- Trzop, E.; Turowska-Tyrk, I. *Acta Crystallogr., Sect. B* **2008**, *64*, 375–382.
- Komarov, I. V. *Russ. Chem. Rev.* **2001**, *70*, 991–1016.
- Tantillo, D. J. *Chem. Soc. Rev.* **2010**, *39*, 2847–2854.
- Bremer, M.; Schotz, K.; Schleyer, P. V. R.; Fleischer, U.; Schindler, M.; Kutzelnigg, W.; Koch, W.; Pulay, P. *Angew. Chem., Int. Ed. Engl.* **1989**, *28*, 1042–1044.
- Laube, T.; Lohse, C. *J. Am. Chem. Soc.* **1994**, *116*, 9001–9008.
- Toda, F.; Tanaka, K.; Stein, Z.; Goldberg, I. *Acta Crystallogr., Sect. C* **1996**, *52*, 177–180.
- Kawai, H.; Takeda, T.; Fujiwara, K.; Inabe, T.; Suzuki, T. *Cryst. Growth Des.* **2005**, *5*, 2256–2260.
- Tsuiji, T. *Adv. Strained Interesting Org. Mol.* **1999**, *7*, 103–152.
- Modern Cyclophane Chemistry*; Gleiter, R., Hopf, H., Eds.; Wiley-VCH: Weinheim, Germany, 2004.
- Xin, D.; Ma, Y.; He, F. *Tetrahedron: Asymmetry* **2010**, *21*, 333–338.
- Cheemala, M. N.; Gayral, M.; Brown, J. M.; Rossen, K.; Knochel, P. *Synthesis* **2007**, *24*, 3877–3885.
- Bartholomew, G. P.; Bazan, G. C. *Acc. Chem. Res.* **2001**, *34*, 30–39.

- (19) Meier, H.; Cao, D. *Chem. Soc. Rev.* **2013**, *42*, 143–155.
- (20) Winberg, H. E.; Fawcett, F. S. *Org. Synth.* **1962**, *42*, 83.
- (21) Hope, H.; Bernstein, J.; Trueblood, K. N. *Acta Crystallogr., Sect. B* **1972**, *28*, 1733–1743.
- (22) Gantzel, P. K.; Trueblood, K. N. *Acta Crystallogr., Sect. B* **1965**, *18*, 958–968.
- (23) Dodziuk, H.; Szymanski, S.; Jazwinski, J.; Marchwiany, M. E.; Hopf, H. *J. Phys. Chem. A* **2010**, *114*, 10467–10473.
- (24) Zhou, X.; Liu, R.; Allinger, N. L. *J. Am. Chem. Soc.* **1993**, *115*, 7525–7526.
- (25) Choi, C. H.; Kertesz, M. *Chem. Commun.* **1997**, *22*, 2199–2200.
- (26) Orimoto, Y.; Aoki, Y. *Int. J. Quantum Chem.* **2002**, *86*, 456–467.
- (27) Dodziuk, H.; Szymanski, S.; Jazwinski, J.; Ostrowski, M.; Demissie, T. B.; Ruud, K.; Kus, P.; Hopf, H.; Lin, S. *J. Phys. Chem. A* **2011**, *115*, 10638–10649.
- (28) Grimme, S.; Muck-Lichtenfeld, C. *Isr. J. Chem.* **2012**, *52*, 180–192.
- (29) Bachrach, S. M. *J. Phys. Chem. A* **2011**, *115*, 2396–2401.
- (30) Quenneville, J.; Germann, T. G. *J. Chem. Phys.* **2009**, *131*, 024313.
- (31) Frisch, M. J.; Trucks, G. W.; Schlegel, H. B.; Scuseria, G. E.; Robb, M. A.; Cheeseman, J. R.; Scalmani, G.; Barone, V.; Mennucci, B.; Petersson, G. A.; Nakatsuji, H.; Caricato, M.; Li, X.; Hratchian, H. P.; Izmaylov, A. F.; Bloino, J.; Zheng, G.; Sonnenberg, J. L.; Hada, M.; Ehara, M.; Toyota, K.; Fukuda, R.; Hasegawa, J.; Ishida, M.; Nakajima, T.; Honda, Y.; Kitao, O.; Nakai, H.; Vreven, T.; Montgomery, Jr., J. A.; Peralta, J. E.; Ogliaro, F.; Bearpark, M.; Heyd, J. J.; Brothers, E.; Kudin, K. N.; Staroverov, V. N.; Kobayashi, R.; Normand, J.; Raghavachari, K.; Rendell, A.; Burant, J. C.; Iyengar, S. S.; Tomasi, J.; Cossi, M.; Rega, N.; Millam, J. M.; Klene, M.; Knox, J. E.; Cross, J. B.; Bakken, V.; Adamo, C.; Jaramillo, J.; Gomperts, R.; Stratmann, R. E.; Yazyev, O.; Austin, A. J.; Cammi, R.; Pomelli, C.; Ochterski, J. W.; Martin, R. L.; Morokuma, K.; Zakrzewski, V. G.; Voth, G. A.; Salvador, P.; Dannenberg, J. J.; Dapprich, S.; Daniels, A. D.; Farkas, Ö.; Foresman, J. B.; Ortiz, J. V.; Cioslowski, J.; Fox, D. J. *Gaussian 09*, Rev. A.02; Gaussian, Inc.: Wallingford, CT, 2009.
- (32) Zhao, Y.; Truhlar, D. G. *Theor. Chem. Acc.* **2008**, *120*, 215–41.
- (33) Grimme, S. *J. Comput. Chem.* **2006**, *27*, 1787–1799.
- (34) Petersson, G. A.; Al-Laham, M. A. *J. Chem. Phys.* **1991**, *94*, 6081–90.
- (35) Peng, C.; Ayala, P. Y.; Schlegel, H. B.; Frisch, M. J. *J. Comput. Chem.* **1996**, *17*, 49–56.
- (36) Hratchian, H. P.; Schlegel, H. B. *J. Chem. Theory Comput.* **2005**, *1*, 61–69.
- (37) Wong, M. W.; Wiberg, K. B.; Frisch, M. J. *J. Comput. Chem.* **1995**, *16*, 385–394.
- (38) Boa, D.; Ramu, S.; Contreras, A.; Upadhyayula, S.; Vasquez, J. M.; Beran, G.; Vullev, V. I. *J. Phys. Chem. B* **2010**, *114*, 14467–79.
- (39) Quantum ESPRESSO is a community project for high-quality quantum-simulation software, based on density-functional theory, and coordinated by Paolo Giannozzi. See <http://www.quantum-espresso.org> and <http://www.pwscf.org>.
- (40) Perdew, J. P.; Burke, K.; Ernzerhof, M. *Phys. Rev. Lett.* **1996**, *77*, 3865–3868.
- (41) See <http://www.physics.rutgers.edu/~dhv/uspp/uspp-cur/Work/006-C/006-C-gpbe-bm/>.
- (42) Kertesz, M.; Hoffmann, R. *J. Solid State Chem.* **1984**, *54*, 313–319.
- (43) Fahy, S.; Louie, S. G.; Cohen, M. L. *Phys. Rev. B* **1986**, *34*, 1191–1199.
- (44) Blanksby, S. J.; Ellison, G. B. *Acc. Chem. Res.* **2003**, *36*, 255–263.
- (45) Mau, A. W. H. *J. Chem. Soc., Faraday Trans. 1* **1978**, *74*, 603–612.
- (46) Wada, A.; Tanaka, J. *Acta Crystallogr., Sect. B* **1977**, *33*, 355–360.
- (47) Harada, J.; Ogawa, K.; Tomoda, S. *Chem. Lett.* **1995**, 751–752.
- (48) Ehrenberg, M. *Acta Crystallogr.* **1966**, *20*, 182–186.
- (49) Dougherty, D. A.; Choi, C. S.; Kaupp, G.; Buda, A. B.; Rudzinski, J. M.; Osawa, E. *J. Chem. Soc., Perkin Trans. 2* **1986**, 1063–1070.
- (50) Battersby, T. R.; Gantzel, P.; Baldrige, K. K.; Sigel, J. S. *Tetrahedron Lett.* **1995**, *36*, 845–848.
- (51) Grimme, S. *Chem.—Eur. J.* **2004**, *10*, 3423–3429.
- (52) Lyssenko, K. A.; Antipin, M. Y.; Antonov, D. Y. *ChemPhysChem* **2003**, *4*, 817–823.
- (53) Staroverov, V. N.; Davidson, E. R. *J. Am. Chem. Soc.* **2000**, *122*, 7377–7385.
- (54) Head-Gordon, M. *Chem. Phys. Lett.* **2003**, *372*, 508–511.